Solar Phys (2020) 295:110
https://doi.org/10.1007/s11207-020-01674-4

Comparative Study and Development of Two Contour-Based Image Segmentation Techniques for Coronal Hole Detection in Solar Images

Sanmoy Bandyopadhyay[1] · **Saurabh Das**[1] · **Abhirup Datta**[1]

Received: 9 March 2020 / Accepted: 21 July 2020 / Published online: 7 August 2020

Abstract The study of solar coronal holes (CHs) is important in the understanding of solar physics and the prediction of space weather events, which have significant impact on space-based instruments, communication and navigation systems. With the availability of the multi-wavelength Atmospheric Imaging Assembly (AIA) instrument on board Solar Dynamics Observatory (SDO) satellite, a large volume of high-resolution solar images are produced continuously. Proper detection of CHs from AIA images is an important issue and recently, a few contour and machine learning-based techniques are found to be promising for such purpose. However, accuracy, time complexity and the requirement of human intervention are some of the critical issues with such methods. In this paper, to address these challenging issues, two contour-based approaches are developed, namely i) the Hough transformed simulated parameterized online region-based active contour method (POR-ACM) and ii) fast fuzzy c-means clustering followed by Hough transformed simulated static contour method (FFCM-SCM). The major issues that are addressed here are automated initialization of contour, reducing time complexity and avoidance of non-coronal hole inside a coronal hole region during contour evolution. The proposed techniques have been tested on three benchmark solar disk images and compared with the existing active contour without edge- (ACWE) based method and fuzzy energy-based dual contour method (FEDCM) of CHs segmentation. The results indicate the capability of the proposed techniques in detection and extraction of CHs in solar disk image with higher accuracy and reduced time complexity.

Keywords Coronal holes · Solar image · Automated detection: circular Hough transform, parameterized online region-based active contour, fast fuzzy c-means

✉ S. Bandyopadhyay
sanmoy1985@rediffmail.com

S. Das
das.saurabh01@gmail.com

A. Datta
abhirup.datta@iiti.ac.in

[1] Discipline of Astronomy, Astrophysics and Space Engineering, Indian Institute of Technology, Indore, Simrol, Indore 453552, India

1. Introduction

The Sun plays a vital role in the space environment and is responsible for many important phenomena such as flares, coronal mass ejection and geomagnetic storms (Gombosi, 1998). CHs are the main source of solar wind and are accountable for geomagnetic storms. The solar wind and the geomagnetic storm directly affect the electronics on artificial satellites, disrupt communication and introduce severe errors in the satellite-based navigation system. Solar wind and geomagnetic storm also cause severe electric supply disruption by affecting the power grids in mid and high latitude locations. Accurate prediction of location and size of CHs are hence important requirements of the scientific community.

For a long time, hand-drawn maps of CHs were the only way to study the CHs (Harvey and Recely, 2002; Krista and Gallagher, 2009; Reiss et al., 2015). However, with the advancement of image processing techniques, a few automated segmentation techniques using magnetograms and spectroscopy data have been used in the last few years for this purpose. Most of the advances in this direction used the data from SDO in different wavelengths. SDO provides a high-resolution image of the solar disk in different wavelengths by AIA instrument.

Local intensity thresholding has been used by Krista and Gallagher for detection of CHs in a solar disk image of wavelength 195 Å (Krista and Gallagher, 2009). This method, however, strongly depends on the proper selection of window size. Rotter et al. (2012) had applied a histogram-based thresholding method for extraction of CHs from 193 Å images. The accuracy of this method, again, depends on the selection of threshold value present in local minima. Further, the success of this method is limited in the case of histogram overlap. Lowder et al. (2014), and Kirk et al. (2009), had also used the thresholding-based segmentation technique for CHs detection. But the main concern associated with the outcome from this technique is the proper distribution of the histogram, which often varies with changes in the wavelength of the solar image and conditions of imaging (Boucheron, Valluri, and McAteer, 2016).

A region-growing-based segmentation technique had also been implemented by Caplan, Downs, and Linker (2016) for mapping of CHs obtained from multi-instrument images. However, the success of the region-growing-based method depends on the proper selection of the seed points in images.

Active contour methods (ACMs) such as the Chan-Vese ACM (C-VACM) have also been used by Boucheron, Valluri, and McAteer (2016). However, this method requires the initialization of the contours within the boundary of the CHs. Moreover, it requires the exact value of solar disk center co-ordinates and radius for the elimination of the off-disk region.

Ciecholewski (2015) used a watershed transformation technique for automated coronal segmentation in solar disk images. But it requires a large variation in color in the image. The method also sometimes results in over-segmentation of the images.

A spatial possibilistic clustering algorithm (SPoCA) has been applied for multiple region detection (CHs, active region and quiet Sun region) in solar disk image using multiple wavelengths (Verbeeck et al., 2014). This method shows good performances, however, is having mathematical complexity due to the use of three different algorithms.

The convolution neural network- (CNN) based technique has also been used for the solar image segmentation purpose (Illarionov and Tlatov, 2018). This method, like any other machine learning technique, requires a large database of solar images for training and testing of the network. Both the CNN-based method (Illarionov and Tlatov, 2018) and the active contour-based method (Boucheron, Valluri, and McAteer, 2016) require down-sampling of the images to reduce the time and computational complexity. However, this also leads to loss of information.

Very recently, a fuzzy energy-based dual contour method (FEDCM) has been introduced by Bandyopadhyay, Das, and Datta (2020) for the CHs detection. The method has the advantage to detect CHs accurately due to the incorporation of fuzzy techniques and the ability to detect the topological changes. However, the method requires the initialization of two contours; one for the segmentation of solar image and another for the extraction of CHs from the segmented image.

Among the stated methods of CHs segmentation contour-based technique is capable of producing smooth and closed contours as segmentation results (Caselles, Kimmel, and Sapiro, 1997). Moreover, it can achieve sub-pixel accuracy of object boundaries (Caselles, Kimmel, and Sapiro, 1997). However, this method of segmentation suffers from two major issues: first, contour initialization and second, the way of solving the optimization function. Boucheron, Valluri, and McAteer (2016) had countered the issue of contour set-up by initializing the contour within the CHs region by means of an intensity thresholding technique. However, in the work a major concern is choosing of the correct threshold value of initializing the contour. In (Boucheron, Valluri, and McAteer, 2016), the authors had applied a heuristic approach to choosing the optimize threshold value. Furthermore, the ACWE technique used in (Boucheron, Valluri, and McAteer, 2016) depends on a gradient descent technique to solve the cost function associated with the technique, which is a very time consuming method. The stated issues have been handled in (Bandyopadhyay, Das, and Datta, 2020), where the authors had used a fuzzy energy-based active contour method (FEACM) for solving the problem CHs segmentation. FEACM has the advantage that the method does not require one to solve the gradient associated with the energy function, like ACWE methods (Krinidis and Chatzis, 2009). Moreover, for contour initialization in the work the authors had used the circular Hough transform technique which has overcome the issue of contour set-up as associated with ACWE technique of CHs detection. But in (Bandyopadhyay, Das, and Datta, 2020) it has been found that only initialization of single contour is unable to solve the CHs extraction problem. So, the FEDCM requires initialization of two contours, one for segmentation of the solar image and another for extraction of CHs from the segmented image. This in turn increases the time complexity of the method.

Thus in order to avoid the issues associated with the contour-based techniques, here we have developed two such approaches for automated detection of CHs based on contour-based techniques which can be solved by initializing single contour only in real time. A fast fuzzy c-means (FFCM) clustering followed by the Hough transformed simulated static contour method (FFCM-SCM) has been proposed for the fast identification of the CHs. Meanwhile a Hough transformed simulated parameterized online region-based active contour method (POR-ACM) has been proposed for improved accuracy in the other methods. The hybrid contour-based clustering approach is faster than the classical active contour approach, while the active contour method is more accurate than the hybrid contour-based clustering technique.

The main contributions in this work of CHs extraction from solar disk image are:

i) Introduction of parameterized real-time contour-based technique for accurate detection of CHs.
ii) Demonstration of a fast technique for CHs detection using a hybrid contour-based clustering technique.

The proposed methods have been applied and tested on few benchmark images of the solar disk. The images of the solar disk had been taken at a fixed wavelength of 193 Å from the SDO/AIA website. The details as regards the images are discussed in the subsequent section of this paper. The results are compared with the existing FEDCM and active contour without

edge (ACWE) method of CHs segmentation algorithms (Boucheron, Valluri, and McAteer, 2016). Further, the results are compared with the synoptic map image and the accuracy of the proposed techniques is evaluated.

The organization for the rest of the paper is as follows. The proposed methodologies of CHs detection are elaborated in Section 2. In Section 3, discussions on the results and findings are carried out. At last, in Section 4, the conclusion on the performance of the proposed work of CHs detection and a comparison with the existing ACWE model of CHs segmentation is drawn.

2. Methodology

2.1. Datasets

The developed algorithms are applied and tested on a few benchmark datasets. The datasets correspond to randomly chosen ((a) *2017-01-30*, (b) *2017-03-14* and (c) *2017-09-14*) solar disk images in fits file format from Joint Science Operations Center (JSOC).[1] These data are AIA level 1 data at observed in extreme ultraviolet (EUV) wavelengths. The AIA instrument captures Sun at several frequencies. The images used for the present work are EUV images of wavelength 193 Å having a resolution of 4096×4096. One image per day has been considered for the work.

2.2. Challenges in CHs Detection

The CHs region is characterized by lower density and temperature than the surrounding plasma. It appears as a low-intensity dark region in X-ray and EUV images of the Sun (Munro and Withbroe, 1972; Krista and Gallagher, 2009; Rotter et al., 2012; Reiss et al., 2015). Thus from the image processing point of view, the task is detecting the lower intensity region. However, an important consideration in the case of solar image processing is removal of the limb effect. From the point of view of image processing, this image contains a region which is not part of the solar disk but has a similar intensity composition of the CHs. Prior limb correction is thus essential in almost all existing algorithms to properly detect the CHs.

The existing techniques such as threshold-based methods are unsatisfactory because fixing the threshold value is a difficult job due to overlapping histograms of the foreground and background and due to change in intensities in different images. Moreover, the clustering techniques used for automated threshold selection also suffer from similar features. The contour-based techniques, on the other hand, use the additional feature of a coronal hole (CH) that it is a closed object. However, one challenging issue in such approaches is to initialize the contour appropriately. The other issue is to overcome the local minima problem.

This paper aims to detect the CHs region in solar disk images with low computational cost without changing the resolution of the considered image. As already mentioned, there exist two important issues in applying contour-based methods in the case of solar images. One is the presence of solar limbs in the solar image, while another is the generation of initial contour. Both issues are simultaneously handled in the present work in a novel strategy by using a Hough transformation. These are presented next.

[1] The data has been collected from http://jsoc.stanford.edu/How_toget_data.html.

2.2.1. *Issue with Solar Limb*

The solar limb is part of the image which appears brighter than the edge of the solar disk due to solar corona. Due to the high-intensity value of this region, all segmentation algorithms fail to eliminate the region and this, in turn, results in misclassification.

There were several techniques that have been proposed to tackle this problem. First limb brightening emendation has been introduced by Barra et al. (2009). The method transforms the image into a polar plane with the origin at the solar disk center. Delouille et al. (2018) had applied solar limb correction in the pre-processing step. Here all pixels with a greater distance than the radius of the Sun $1R_{\odot}$ from the center of the solar disk are withdrawn and the remaining pixels are rectified for limb brightening effects. In (Reiss et al., 2015), the limb brightening effect has been corrected by fitting a smooth transition function and inverting it. In CHs segmentation using CNN, prior segmentation of the solar disk had been applied (Illarionov and Tlatov, 2018) and maximal intensity has been set for the pixels outside the solar disk. Boucheron, Valluri, and McAteer (2016) had applied the limb-brightening rectification as described by Verbeeck et al. (2014) before all posterior processing of the solar image. Nieniewski (2004) had set two rings (inner and outer) of intensity values 255, based on the Bresenham algorithm (Bresenham, 1965). In this experiment, the radii of the circles were set at 186 and 188 pixels, respectively (Nieniewski, 2004). The area inside the circles was replenished and the borders were smoothed out by image morphological operation with a structuring element of size 3×3 pixels. This set-up prevents the leaking in the merging process (Nieniewski, 2004).

However, most of the stated techniques of limb correction require accurate data about the co-ordinate points of solar disk center and the length of the solar radius in the image.

2.2.2. *Issue with Contour Initialization*

Contour initialization is a vital problem in the contour-based method as the overall performance and accuracy of the method depend on it. In general, the contour should be initialized within the region of interest (RoI) (Wang et al., 2017; Darolti et al., 2008; Xingfei and Jie, 2002; Huang and Zeng, 2015) and requires human supervision. To overcome this problem many researchers had introduced different strategies such as initializing the contour near the image boundary, setting the contour outside RoI and contour initialization free ACM (Chan and Vese, 2001; Xie and Mirmehdi, 2010). However, for the task of CHs extraction in the solar image, there is a high probability of including the unwanted pixels as the CHs regions which are not part of the solar disk. Moreover, the background region in solar disk images having the same color composition as that of the RoI, there is a high possibility that both CHs regions and background in solar disk images are classified as CHs. Boucheron, Valluri, and McAteer (2016) had tackled this contour set-up issue by initializing the contour within the CHs region using an intensity thresholding method. But choosing the correct threshold value is still a major concern. Recently, Bandyopadhyay, Das, and Datta (2020) introduced a circular Hough transform-based technique to solve this issue. However, single circular contour initialization is not capable to segment the CHs properly (Bandyopadhyay, Das, and Datta, 2020).

In order to overcome the above-mentioned problems of contour initialization, misclassification due to solar limb, and real-time analysis of CHs region in a solar disk image, in this work, circular Hough transform driven single contour-based CHs detection techniques are introduced. The Hough transform has the capability to detect a circular object in a noisy image (Duda and Hart, 1972; Yuen et al., 1990; Hough, 1962). Furthermore, the main aim

of this work is to extract the CHs region in the solar disk, and the solar disk is circular in shape when presented in the two-dimensional (2D) image; as such, a circular Hough transform[2] is used here. The detected circle with radius r and center (a, b) is considered as the initial circular contour for both proposed methods, POR-ACM and FFCM-SCM. Details as regards the circular Hough transform-based contour initialization have been discussed in (Bandyopadhyay, Das, and Datta, 2020).

2.3. Proposed CHs Detection Methods

2.3.1. POR-ACM

After the detection of the solar disk region using the initialized Hough transformed inspired circular contour, the unwanted regions (which include solar limbs and image background) has been eliminated by replacing the corresponding pixels intensity value with white pixel intensity. This elimination of the unwanted pixels has been done with the knowledge that the circular contour has been initialized on the boundary of the solar disk, the region inside the boundary is the solar disk portion of the image and the region outside the initial contour is an off-disk region. This elimination of a region, in turn, will help in reducing computational complexity and misclassification of the region.

The POR-ACM is based on an online region-based active contour method (OR-ACM). The main advantage of using OR-ACM is that the method is computationally fast and is applicable for real-time detection of the CHs. Moreover, the method is mathematically less complex than other ACM-based object detection algorithm and does not require any parameter tuning (Talu, 2013). However, OR-ACM has the probability to get stuck at local minima and thus give rise to many small regions (Talu, 2013), and it is also stuck on the object boundary due to strong edge and presence of local minima. As such the method misclassifies RoI which is situated inside another object present in the image. In order to handle this, a post-processing operation of morphological opening and closing has been incorporated in the work of (Talu, 2013). A parametric-signed pressure function has been introduced to address the problem where RoI is inside another object.

The contour level set updating is given by (Talu, 2013)

$$\frac{\partial \phi}{\partial t} = H(\mathrm{spf}(I(t)))\phi(t). \tag{1}$$

Here, in Equation 1 the term $\phi(t)$ denotes the level set function of the curve at iteration t whose initial formulation is given by

$$\phi = -\sqrt{(x-a)^2 + (y-b)^2} + r. \tag{2}$$

The term H in Equation 1 indicates the Heaviside or the unit step function. The notion $\mathrm{spf}(I(t))$ denotes the region-based signed pressure function of an image at iteration t (Zhang et al., 2010). The signed pressure function of image I is given by

$$\mathrm{spf}(I(x,y)) = \frac{I(x,y) - \frac{c_1+c_2}{2}}{\max\left(\left|I(x,y) - \frac{c_1+c_2}{2}\right|\right)}, \tag{3}$$

[2]Details about the outcome obtained after applying the circular Hough transform are discussed in the Appendix.

Algorithm 1 Proposed POR-ACM.

Input: Image I
Initialization: $\text{Area}_1 = 0$, $\text{Area}_2 = 0$, $A_d = 0$, and other parameters
Initialize circular contour using circular Hough transform
Eliminate off-disk region / region outside the circle
Calculate Area_1 by determining total number of pixels inside the contour
for iter=1:max_iter **do**
    Update contour position based on pspf(I(x, y))
    Calculate Area_2, the total pixels inside the contour
    Calculate $A_d = |A_2 - A_1|$
    if $A_d = 0$ **then**
        goto Step *16*
        break;
    else
        $A_1 \longleftarrow A_2$
        goto Step *6*
Output: The location with $\phi(\text{iter}) > 0$ are CHs pixels for image I.

where the terms c_1 and c_2 represent the mean intensity values inside and outside the curve, respectively.

The stopping criterion for the OR-ACM is given by the formulation

$$\int H(\phi(t)) - \int H(\phi(t-1)) = 0, \tag{4}$$

where the terms $H(\phi(t))$ and $H(\phi(t-1))$ denote the total energy at iterations t and $(t-1)$.

The parametric-signed pressure function 5 is given by

$$\text{pspf}(I(x,y)) = \frac{I(x,y) - \frac{\alpha_1 c_1 + \alpha_2 c_2}{2}}{\max\left(\left|I(x,y) - \frac{\alpha_1 c_1 + \alpha_2 c_2}{2}\right|\right)}, \tag{5}$$

where the parameters α_1 and α_2 indicate the weight parameter for the mean intensity inside and outside the curve, respectively. These parameters generate an extra force on the curve so that it does not get stuck at the local minima present within the strong edge of the object. The corresponding algorithm of the proposed POR-ACM is given in Algorithm 1.

2.3.2. FFCM-SCM-Based CHs Segmentation

In the second approach, the fast fuzzy clustering along with the SCM has been used to detect the CHs. In the first stage of this technique, FFCM has been introduced in order to segment the image into CHs and non-CHs regions by taking global statistics of the image, i.e., the histogram of the image pixels' intensities has been considered in place of raw image data (Semechko, 2019). The cost function for a classical fuzzy c-means (FCM) algorithm is given by Equation 6 (Bezdek, Ehrlich, and Full, 1984);

$$J_E = \sum_{j=1}^{N} \sum_{i=1}^{c} {\mu_{ij}}^m \left|\left| p_j - \upsilon_i \right|\right|^2. \tag{6}$$

Here μ is the membership function of the jth pixel intensity p_j, in the ith cluster. The term N denotes the total number of pixels in the image, c indicates total cluster number and m is the fuzziness constant. The term υ denotes the cluster center, which is given by

$$\upsilon_i = \frac{\sum_{j=1}^{N} {\mu_{ij}}^m p_j}{\sum_{j=1}^{N} {\mu_{ij}}^m}, \tag{7}$$

where the membership function μ_{ij} is initially denoted by

$$\mu_{ij} = \sum_{k=1}^{c} \left(\frac{||p_j - \upsilon_i||}{||p_j - \upsilon_k||} \right)^2. \tag{8}$$

In FFCM (Semechko, 2019), the raw data term p_j has been replaced by n_l. Here the term n_l indicates the number of the occurrence of pixels intensity value l. Thus, the overall cost function for FFCM is given by

$$J_E = \sum_{l=0}^{255} \sum_{i=1}^{c} {\mu_{il}}^m \, ||n_l - \upsilon_i||^2. \tag{9}$$

As such, Equations 7 and 8 can be rewritten as

$$\upsilon_i = \frac{\sum_{l=0}^{255} {\mu_{il}}^m n_l}{\sum_{l=0}^{255} {\mu_{il}}^m}, \tag{10}$$

where μ_{il} is the modified membership value for FFCM-based clustering, which is denoted by

$$\mu_{il} = \sum_{k=1}^{c} \left(\frac{||n_l - \upsilon_i||}{||p_l - \upsilon_k||} \right)^2. \tag{11}$$

After the clustering image into two segments, namely foreground (CHs regions and solar image background) and background (non-CHs regions), the original solar image is used to initialize a static contour based on a circular Hough transform. This static contour has been initialized with a view to overcoming the effect of the solar limb and to separating the detected foreground region. The following three conditions can then easily identify the CHs as mentioned below:

i) If the foreground region is present outside the contour, set as background.
ii) Background region is present within the contour, set as background.
iii) The foreground region is present inside the contour, set as foreground CHs regions.

Algorithm 2 highlights the corresponding algorithm of the proposed method FFCM-SCM.

2.4. Validation

In order to validate the proposed techniques, the synoptic maps of the solar surface drawn each day by SWPC forecasters considered as benchmark ground-truth data for the comparison purpose (Boucheron, Valluri, and McAteer, 2016; Illarionov and Tlatov, 2018). Synoptic maps provide forecasters with a broad outline of solar surface features.[3] These maps have

[3]Synoptic map has been collected from https://www.swpc.noaa.gov/products/solar-synoptic-map.

Algorithm 2 Proposed FFCM-SCM.

Input: Image I
Initialization: Randomly initialize membership matrix μ_{il}, threshold ϵ
Calculate image histogram
for iter=1:max_iter **do**
    Calculate cluster center υ_i
    Update membership value using
        $\mu_{il} = \sum_{k=1}^{c} \left(\frac{||n_l - \upsilon_i||}{||p_l - \upsilon_k||} \right)^2$
    if $J_E < \epsilon$ **then**
        goto Step *12*
        break;
    else
        goto Step *4*
Cluster image I into foreground and background
Initialize circular contour ϕ using circular Hough transform
if $\phi(1) > 0$ & pixels labeled foreground **then**
    Label pixel ⟵ foreground
else if $\phi(1) > 0$ & pixels labeled background **then**
    Label pixel ⟵ background
else $\phi(1) < 0$ & pixels labeled foreground
    Label pixel ⟵ background
Output: foreground pixels are CHs pixels for image I.

been produced daily by SWPC forecasters since 1972. The map shows neutral lines, coronal hole boundaries, active regions, plages, filaments, and prominences. The outcome of the proposed POR-ACM and FFCM-SCM techniques[4] have been compared with the CHs segmentation results obtained using the ACWE method (Boucheron, Valluri, and McAteer, 2016) and FEDCM,[5] concerning the ground-truth data. The proposed method has been validated in terms of visual analysis, quantitative analysis based on segmentation metrics and the time taken to generate the results.

3. Results and Discussions

3.1. Data Pre-Processing

The SDO/AIA image obtained from the fits file is not suitable for the purpose of image segmentation in its original form. This may be due to the fact that the original SDO/AIA images are either too dim or too bright.[6] The main reason for this is the linear scaling of the data between the minimum and maximum pixels values. Moreover, the variance of the original image is also high, of the order of 10^4. Along side, the image resolution is too high to meet the real-time execution. As such, to make the image suitable for the real-time image

[4]Corresponding code for POR-ACM and FFCM-SCM are available on github https://github.com/sanmoy1985/CoronalHolesContour.

[5]Code of FEDCM is available in https://github.com/sanmoy1985/CoronalHolesFuzzyContour.

[6]Original text available in https://www.uclan.ac.uk/sdo/assets/sdo_primer_V1.2.pdf.

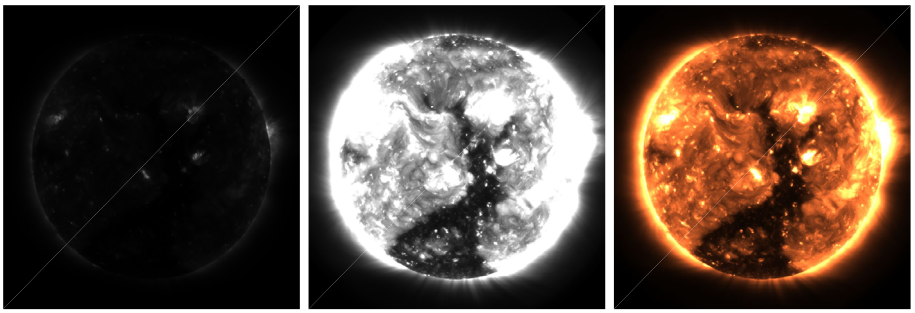

Figure 1 Here (**a**) shows the original image, (**b**) indicate the linear scaled image obtained for supplied range of [0, 255] and (**c**) shows the light brown colorized solar image obtained from the solar fits file captured on *2017-01-30*.

segmentation task the image data in the fits file has been resized to 1024×1024, after the data having been passed through a pre-processing step. In the present work, the pixel value has been pre-processed using three separate techniques to fulfill three different criteria.

For the task of CHs segmentation using POR-ACM the pixels value has been normalized using Equation 12:

$$I_{\text{norm}}(x, y) = \frac{I(x, y) - \min(I(x, y))}{\max(I(x, y)) - \min(I(x, y))}, \tag{12}$$

where $I_{\text{norm}}(x, y)$ denote the normalized pixels value, and the term $\max(I(x, y))$ and $\min(I(x, y))$ represent the maximum and minimum pixel intensity of the original fits file data, respectively. However, this process of pre-processing generates images with a very low variance, in the order of 10^{-8}. Thus, in order to overcome this, the normalized pixels value has been multiplied with the factor of 255.

On the other hand, the algorithm of FFCM-SCM requires the value of image pixels to lie between 0 to 255. At the same time, the previous image pre-processing technique generates an image with low variance. As such, the FFCM-SCM technique will have the tendency to detect all the low-intensity region as the CHs. The fuzzy technique has the property to detect an ambiguous region even if the image does not contain proper region boundary. To tackle this, in the pre-processing step for FFCM-SCM, the image has been linearly scaled between the pixels value of 0 to 255. The method will scales the image in such a way that any pixels value below 0 is assigned to black and any values above 255 is assigned to white. Values 0 to 255 are linearly scaled as indicated by different gray levels.

At last for the displaying purpose the fits file image has been typically colorized in light brown for easy visualization and making it suitable for the visual identification of CHs.[7] The resultant image obtained using three different pre-processing techniques are shown in Figure 1 and the corresponding code has been made available in github.[8]

[7]Details about SDO/AIA 193 Å visualization can be found in https://www.nasa.gov/content/goddard/sdo-aia-193-angstrom/.

[8]Code for SDO/AIA image pre-processing is available in https://github.com/sanmoy1985/CoronalHolesContour/blob/master/Fits2Image.m.

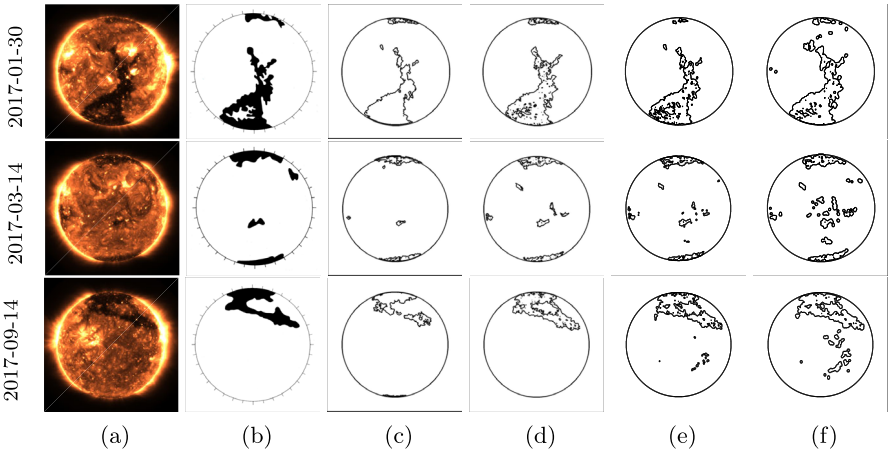

Figure 2 A pictorial summarization of comparative studies between existing algorithm and the proposed methods, where (**a**) original image, (**b**) ground-truth image (generated-based on synoptic map image), and outputs from (**c**) ACWE (**d**) FEDCM (**e**) POR-ACM and (**f**) FFCM-SCM are shown.

3.2. Parameter Settings

There are mainly two parameters which control the outputs of the POR-ACM-based coronal hole segmentation; α_1 and α_2. These parameters control the foreground and the background consistency. If these parameters are not properly chosen then there is a probability that some CHs regions get classified as non-CHs and vice versa. So, for this work the parameter α_1 has been kept between $[0.5, 0.1]$, while the parameter α_2 has been kept within the interval of $[0.1, 0.01]$. On the other hand, the fuzziness value of m is a vital factor for FFCM-SCM technique. The lower the value of m, the more it will act like a classical c-mean cluster technique. As such for convenience of this work, in this case m has been assigned the value of 20.

3.3. Visual Analysis

The solar disk images used for the experimental purpose and corresponding results of CHs extraction obtained using the proposed methods and existing ACWE-based techniques are shown in Figure 2. From visual comparison shown in Figure 2, it can be seen easily that the output obtained using the proposed techniques and FEDCM generates comparable results to that of the ground truth based on synoptic maps information. Meanwhile the output generated using the ACWE method has under segmented the RoI.

From the image in the first row of Figure 2c, and from the enlarged images in Figure 3, it can be noted that the ACWE method fails to detect the non-coronal whole region which is present within RoI as shown in the synoptic map image. However, this non-CHs region can also be noticed in the original image. Now, while comparing with the outcomes obtained using the POR-ACM, it can be seen that the proposed method has better detected the non-CHs region lying within the coronal hole region. A similar thing can be found for the output obtained using FFCM-SCM and FEDCM.

From the results shown in the second row of Figure 2 and from the enlarged images in Figure 4, it can be easily noticed that the FFCM-SCM-based method generates about the same results as shown in the ground-truth image. This also holds true for the case of the

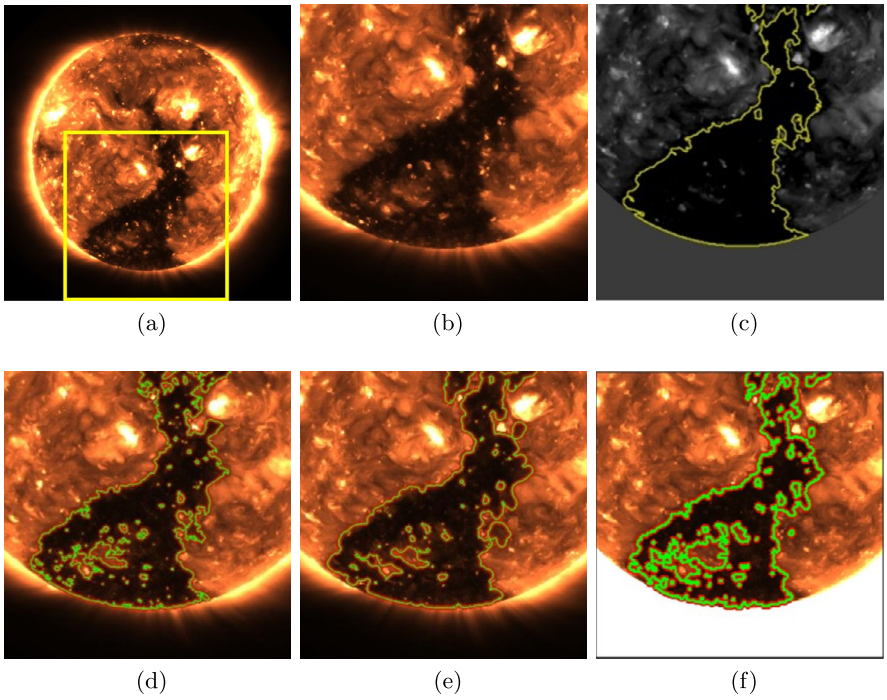

Figure 3 Enlarge image showing performance of different contour-based segmentation technique on image dated *2017-01-30* when non-CHs regions are present within CHs region. Here (**a**) shows the original image, (**b**) indicate the enlarge region located within highlighted square in (**a**), the segmentation output obtained by using ACWE, FEDCM, FFCM-SCM and POR-ACM have been shown in (**c**)–(**f**) respectively.

proposed POR-ACM- and FEDCM-based CHs segmentation. However, in the case of an existing ACWE-based technique, it has been found that the method fails to extract all the CHs region from the solar image, particularly the coronal hole region present at the side of the solar disk as shown in Figures 2 and 4. But, from the analysis of Figure 2, it has been also found that both FEDCM, FFCM-SCM and POR-ACM-based techniques have also included some extra regions in the CHs class, which are not highlighted in the ground-truth image. This is because these regions have the same intensity consistency as that of CHs regions. Moreover, it can be found that in the middle of the solar disk there lie CHs as shown in the synoptic map image, this region has been better detected in the output obtained using POR-ACM and FFCM-SCM.

Again from the outcome shown in the third row of Figure 2 and from the enlarged images in Figure 5, it can be noticed that FEDCM and the proposed POR-ACM are able to detect the exact CHs region as shown in the synoptic map. The other two methods, namely the FFCM-SCM- and ACWE-based methods, seem to over-segment and under-segment the solar image, respectively. In a like manner the output is obtained after applying contour-based segmentation techniques on the image in the first row of Figure 2a, in this case nearly a similar type of result has been obtained. The proposed techniques are able to extract the non-CHs region lying within the CHs region in this case also. However, the ACWE-based method fails to extract the same.

The main reason for the success of FEDCM- and POR-ACM-based CHs segmentation is the ability of the ACM to cope with small topological changes that exist within the image.

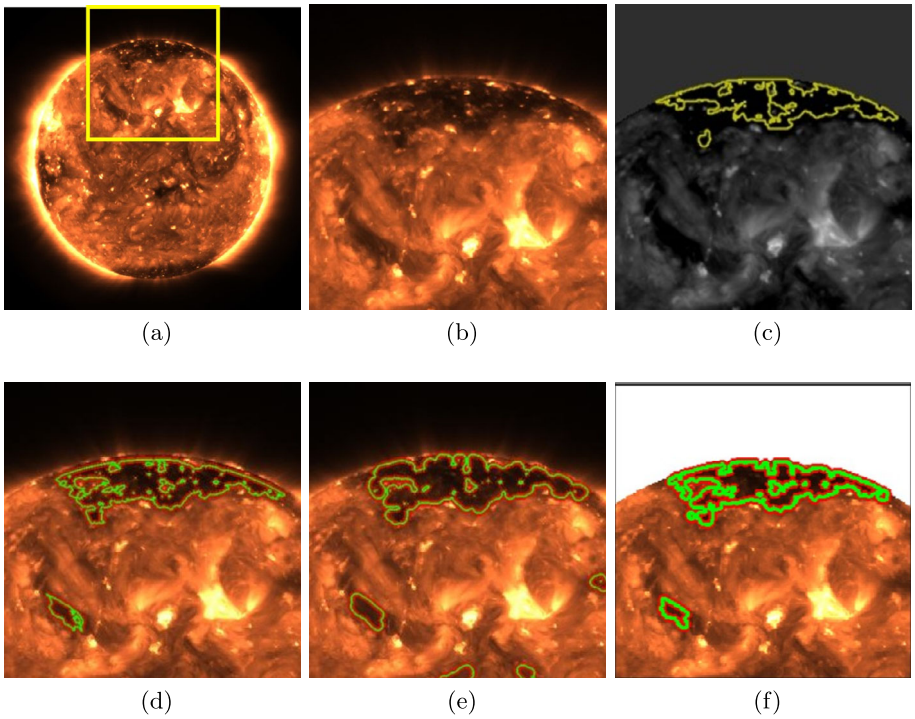

Figure 4 Enlarge image showing performance of different contour-based segmentation technique on image dated *2017-03-14*. Here (**a**) shows the original image, (**b**) indicate the enlarge region located within highlighted square in (**a**), the segmentation output obtained by using ACWE, FEDCM, FFCM-SCM and POR-ACM have been shown in (**c**)–(**f**) respectively.

Furthermore, FEDCM is also incorporated with the advantage of the fuzzy clustering technique which has the capability to detect the ambiguous boundary in the image. As such, the FEDCM technique performs better in few cases. On the other hand, the caliber of extraction CHs using FFCM-SCM is due to the association of the FCM technique with the overall method. The FCM-based clustering method has the higher competence to detect objects having an ambiguous boundary over other methods.

It can be visually noticed that the FFCM-SCM method has detected a few smaller non-CHs regions present inside the solar disk image as CHs which the other methods are unable to localize. This is due to the use of a fuzzy-based technique which can classify the RoI with vague boundaries. The class memberships values for CHs and non-CHs regions and corresponding class assignment are shown in Figure 6. From Figure 6 it can be seen easily that the FFCM clustering technique has identified the CHs region intensity distribution (represented by the red color line) with the highest membership value below the intensity value of 50. At the same time, pixels with the intensity value greater than 50 have been clustered as a non-CHs region (represented by the green color line).

3.4. Image Morphological Operation

While comparing with ground-truth images, it can be observed that in Figures 2–5 both POR-ACM and FFCM-SCM have segmented many small and narrow redundant dark regions along with the CHs. These are the filament regions of the solar image, which are

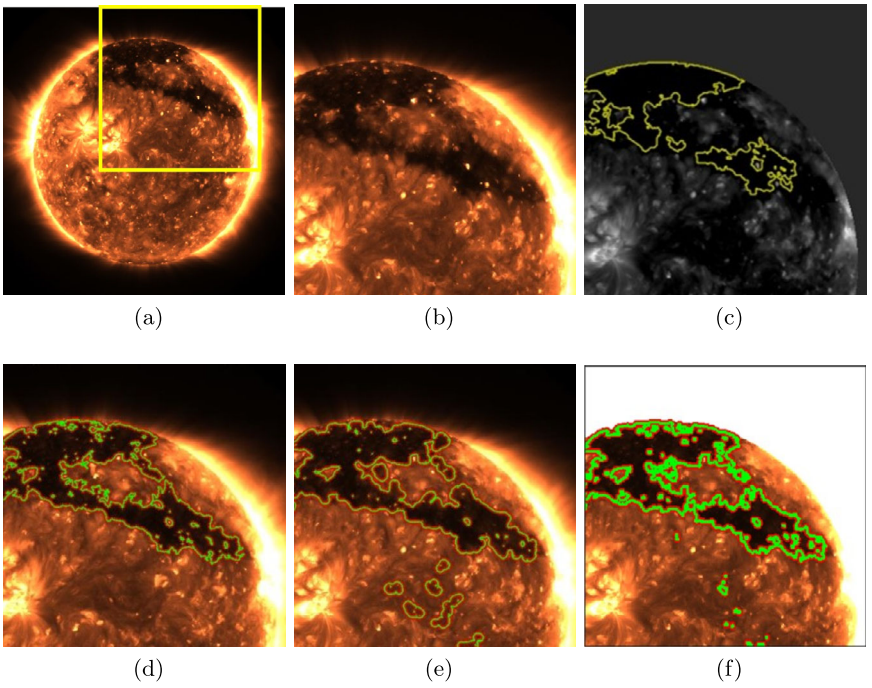

Figure 5 Enlarge image showing performance of different contour-based segmentation technique on image dated *2017-09-14* when non-CHs regions are present within CHs region. Here (**a**) shows the original image, (**b**) indicate the enlarge region located within highlighted square in (**a**), the segmentation output obtained by using ACWE, FEDCM, FFCM-SCM and POR-ACM have been shown in (**c**)–(**f**), respectively.

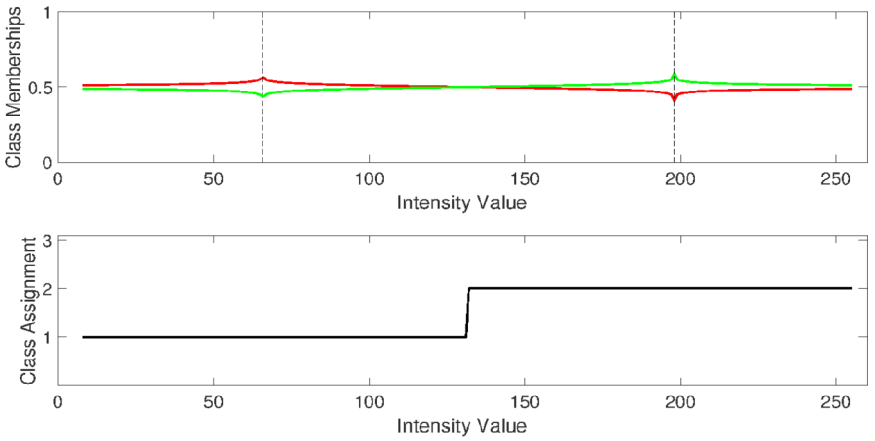

Figure 6 The class memberships value and corresponding class assignment obtained using the FFCM technique for CHs detection.

characterized by a smaller area and are narrower in shape than the CHs region (Boucheron, Valluri, and McAteer, 2016; Reiss et al., 2014). This ultimately affects the accuracy of CHs

region detection. A combination of morphological or magnetic criteria can be used to eliminate these regions from the segmented image (Boucheron, Valluri, and McAteer, 2016). But using magnetic criteria will require an HMI image as an additional information. This in turn will affect the computational time. Thus, to avoid these redundant pixels obtained after implementation of both techniques and to avoid the computational time requirement, a post-processing operation of morphological image processing methods has been introduced. In a post-processing operation, morphological opening is followed by morphological closing. The opening operation dilates the eroded image, using the same structuring element, SE_1, throughout the operations. On the other hand, the closing operation erodes the dilated image, using the same structuring element, SE_2, throughout the closing operations. Thus for output image A the opening operation with structuring element SE_1 is denoted by

$$A \circ \mathrm{SE}_1 = (\mathrm{A} \ominus \mathrm{SE}_1) \oplus \mathrm{SE}_1, \tag{13}$$

and the morphological closing operation with structuring element SE_2 is given by

$$A \bullet \mathrm{SE}_2 = (\mathrm{A} \oplus \mathrm{SE}_2) \ominus \mathrm{SE}_2. \tag{14}$$

Here, in Equations 13 and 14, $(A \ominus \mathrm{SE}_1)$ indicates a morphological erosion operation, while $(A \oplus \mathrm{SE}_2)$ indicates a morphological dilation operation.

In the post-processing scenario, the size of the structuring elements plays an important role in overcoming the redundant pixels from the image. In this work, the radius of the structuring element SE_1 has been kept at 5 throughout the experiment, while the radius of the structuring element SE_2 has been kept within the interval of $[4, 8]$. The segmentation outputs obtained for different radius of the structuring element SE_2 are shown in Figure 7. From the experiment, it can be stated that this method reduces the erroneous detection of filament channels, while not eliminating them entirely.

3.5. Quantitative Analysis

The outcomes from the four methods are analyzed in terms of a segmentation quality score. The Dice coefficient and Jaccard index are used as a matrix to measure the quality score. For the purpose the ground-truth generated from the synoptic map has been taken into account for determining the stated quality scores. The Dice coefficient is given by

$$\mathrm{DC} = \frac{2|\mathrm{A} \cap \mathrm{G}|}{|\mathrm{A}| + |\mathrm{G}|}, \tag{15}$$

where A is the output image obtained after applying the segmentation technique and G is the ground-truth image. The Jaccard index is represented by

$$\mathrm{JI} = \frac{\mathrm{DC}}{(2 - \mathrm{DC})}. \tag{16}$$

From Table 1 it can be noticed that the proposed methods show the suitability in the detection of CHs in the image. It can be concluded that, for most the images, FEDCM-based segmentation provides better output than the other three methods. This is due to the fact that the FEDCM technique can handle topological changes like ACM while it has the capability to tackle vagueness associated with the image due to the presence of fuzzy energy term in the cost function (Bandyopadhyay, Das, and Datta, 2020). The segmentation quality score

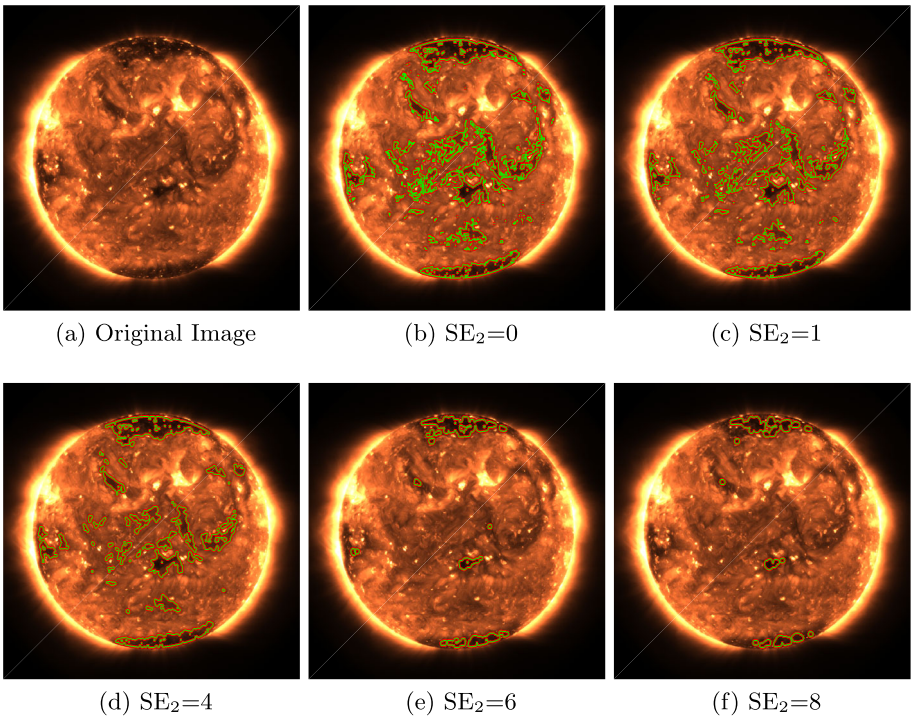

Figure 7 Output obtained after application of an image morphological operation using structuring element (SE_2) of different radius.

Table 1 Coronal holes segmentation quality score.

Images	Measurement metrics	Methods			
		ACWE	FEDCM	POR-ACM	FFCM-SCM
2017-01-30	Dice Coefficient	0.7020	0.7576	0.7437	0.7353
	Jaccard Index	0.5408	0.6098	0.5920	0.5814
2017-03-14	Dice Coefficient	0.5047	0.5998	0.5883	0.5234
	Jaccard Index	0.3375	0.4284	0.4167	0.3545
2017-09-14	Dice Coefficient	0.7066	0.8166	0.7950	0.7157
	Jaccard Index	0.5463	0.6901	0.6597	0.5573

of POR-ACM stood the second highest over the other three discussed techniques, for CHs detected on *2017-01-30*, *2017-03-14* and *2017-09-14*. Moreover, due to the incorporation of a post-processing step based on the segmented region area size, FEDCM has eliminated most of the redundant region as can be found in the output obtained using POR-ACM and FFCM-SCM.

3.6. Execution Time Analysis

The comparison has also been carried out in terms of execution time as shown in Table 2. An investigation has been conducted on a system having been configured with Intel(R)

Table 2 Time and iteration for execution of coronal holes segmentation technique.

Images	Methods							
	ACWE on Image size (512 × 512)		FEDCM on Image size (1024 × 1024)		POR-ACM on Image size (1024 × 1024)		FFCM-SCM on Image size (1024 × 1024)	
	Time (sec)	Iteration	Time (sec)	Iteration	Time (sec)	Iteration	Time (sec)	Iteration
(a) 2017-01-30	141.7941	3	58.2901	10	71.9788	5	57.9049	–
(b) 2017-03-14	141.6941	3	59.3454	10	98.7736	6	45.6274	–
(c) 2017-09-14	141.7132	3	54.8045	10	99.1384	7	51.9919	–

Core(TM)i5-8250U CPU, having the base speed of 1.8 GHz and 4 GB RAM, along with Windows 10, a 64-bit operating system. It has been found that both proposed methods and FEDCM are faster than the ACWE technique. The main reason for the large time taken by the ACWE method, even for low-resolution images, is the presence of a gradient term in its equation. Moreover the method uses a gradient descent technique for optimization of the energy function (Chan and Vese, 2001). This requires a huge computational time. For the case of POR-ACM, it can be found that the method takes quite less time than ACWE, however, the number of iterations is higher. The main reason for the increase in the number of iterations is the contour initialization procedure and the minima searching procedure. The execution time taken by a circular Hough transform to initialize the contour on solar disk boundary is an issue, which also holds true for the case of FFCM-SCM. However, from Table 2 it can be easily noticed that FFCM-SCM takes less time for execution than both the POR-ACM and the ACWE method of CHs segmentation. Moreover, it takes zero iteration to generate the outputs, without compromising the original image resolution. At the same time, it can be seen that FEDCM has comparable performance with that of FFCM-SCM in terms of the execution time taken.

3.7. Magnetic Unipolarity

Unipolarity of the magnetic field within CHs has also been considered for measuring the accuracy of CHs detection, as used in (Boucheron, Valluri, and McAteer, 2016). At time closest to the observational time of the SDO/AIA image, the Helioseismic and Magnetic Imagery (HMI) magnetogram data correspond to the segmented region obtained in SDO/AIA image has been considered for the calculation purpose. The skewness of the flux distribution of magnetogram pixels values located within the detected CHs region is used to measure the related flux imbalance. The average absolute skewness $|\overline{S}|$ of the magnetic field located within the segmented CHs region is computed as $\text{skewness(mag)} = \text{E}(\text{mag} - \overline{\text{mag}})^3/\sigma^3$, where $\overline{\text{mag}}$ is the mean value of the magnetic field strength within the CHs region, σ is the standard deviation, and $E(\cdot)$ is the expectation operator. Thus, while calculating the absolute skewness of each of the R disjoint regions obtained in the segmentation output, the corresponding HMI magnetogram data is taken into account (Boucheron, Valluri, and McAteer, 2016). The absolute skewness of each of the R disjoint regions is given by

$$|S_q| = \text{skewness}(\text{abs}(\text{H}'(\text{x}'', \text{y}''))|(\text{x}'', \text{y}'') \in \text{C}_\text{i}), \text{q} = 1.2, 3, \ldots, \text{R}, \tag{17}$$

where H' is the geometrically transformed HMI magnetogram and C_i is the final contour obtained using the segmentation algorithm. So, the average absolute skewness $|\overline{S}|$ is the

Table 3 The average absolute skewness values obtained for different coronal hole segmentation techniques.

Images	Methods			
	ACWE	FEDCM	POR-ACM	FFCM-SCM
2017-01-30	0.0004	0.0004	0.0006	0.0003
2017-03-14	0.0013	0.0014	0.0020	0.0004
2017-09-14	0.0007	0.0006	0.0007	0.0012

average $|S_q|$ weighted by area:

$$|\overline{S}| = \frac{\sum_{q=1}^{R} |S_q|}{|C_i|}. \tag{18}$$

If the final segmentation output is truly representative of the CHs, then it is expected that $|\overline{S}|$ is large, indicating unipolar magnetic fields. The obtained skewness value has been highlighted in Table 3. From the table it can be found that the POR-ACM-based technique shows the highest skewness value for the solar images taken on *2017-01-30* and *2017-03-14*, and has the second highest performance for the rest of the cases.

3.7.1. HMI Image Alignment

The major issue associated with the calculation of magnetic unipolarity is the alignment of two images, SDO/AIA and solar HMI under consideration. Since these data are observed from different sources there is a high probability of misalignment among this images, as can be observed from the images shown in the first row of Figure 8. This leads to the improper generation of the skewness values. In order to overcome this, the two images are to be put in the same reference frame. For this purpose, in this work's image an interpolation technique has been implemented. The main motive is to distort an image from one pixel grid to another. To interpolate the image, a bilinear interpolation method has been used. As the name suggested the interpolation technique involves two separate linear interpolations. First in one direction, then again in a different direction. Thus the interpolated image for an HMI magnetogram $H(x, y)$ is given by

$$\begin{aligned} H'(x', y') = {} & H(x, y)(1 - \Delta x)(1 - \Delta y) + H(x + 1, y)\Delta x(1 - \Delta y) \\ & + H(x, y + 1)(1 - \Delta x)\Delta y + H(x + 1, y + 1)\Delta x \Delta y, \end{aligned} \tag{19}$$

where Δx and Δy are the fractional parts of row and column locations defined by

$$(\Delta x, \Delta y) = (x_f - x, y_f - y). \tag{20}$$

The term (x_f, y_f) represents the fractional location of the image under consideration from which to sample the output pixel (x, y), which is given by

$$x_f = [(1, \ldots, X') \cdot S] \tag{21}$$

and

$$y_f = [(1, \ldots, Y') \cdot S]. \tag{22}$$

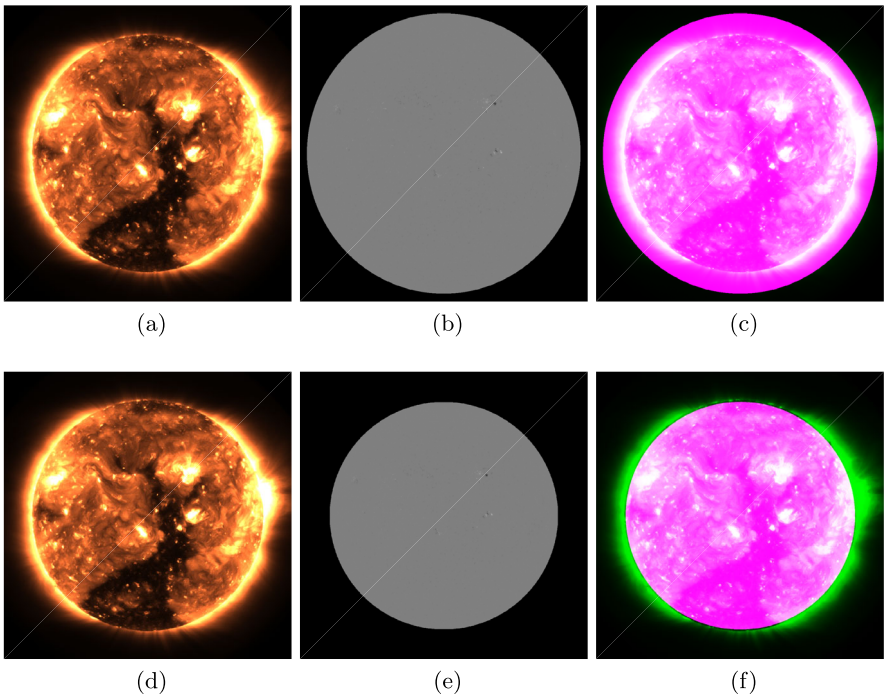

Figure 8 Here (**a**) and (**d**) shows SDO/AIA 193 Å image, (**b**) shows the SDO/HMI image, (**c**) indicated overlap result of the original SDO/AIA and SDO/HMI image (**e**) show the HMI image obtained after bilinear interpolation and (**f**) overlap image obtained after alignment of SDO/AIA and SDO/HMI image obtained for the solar fits file captured on *2017-01-30*.

The term S indicates the scaling factor defined by

$$S = \frac{\mathrm{R}_{\odot} \text{ in AIA image}}{\mathrm{R}_{\odot} \text{ in HMI image}}, \tag{23}$$

where $R_{\odot}$ stands for the radius of the sun and X' and Y' indicate the total numbers of rows and columns in the sampled image, given by X/S and Y/S, respectively. The results obtained after aligning of the AIA and the HMI image are shown in the second row of Figure 8.

Meanwhile, there may exist an angle between the y-axis relative to the north direction which is indicated by the term CROTA2 in the header of the fits file. In order to correct this, a bilinear transform is implemented to express x' and y' as functions of x'' and y''. For this transformation the image has been rotated over $-\Theta$, where $\Theta = \mathrm{CROTA2}$. Thus x'' and y'' can be expressed as

$$x'' = x' \cos(\Theta) + y' \sin(\Theta), \tag{24}$$

$$y'' = -x' \sin(\Theta) + y' \cos(\Theta). \tag{25}$$

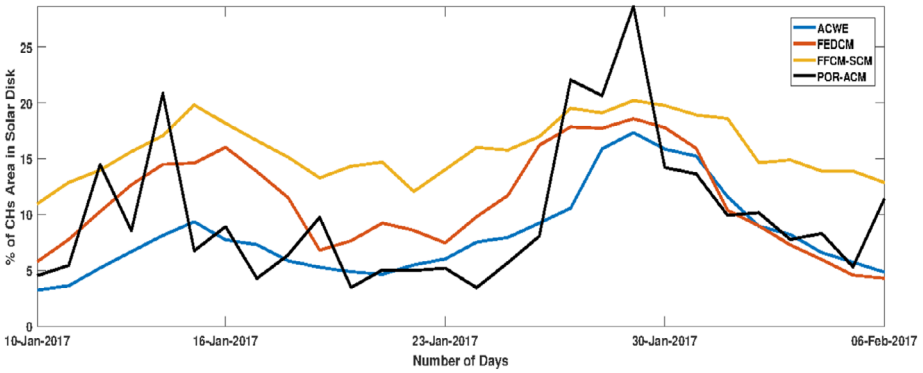

(a) Percentage of CHs area in solar disk during a Carrington rotation.

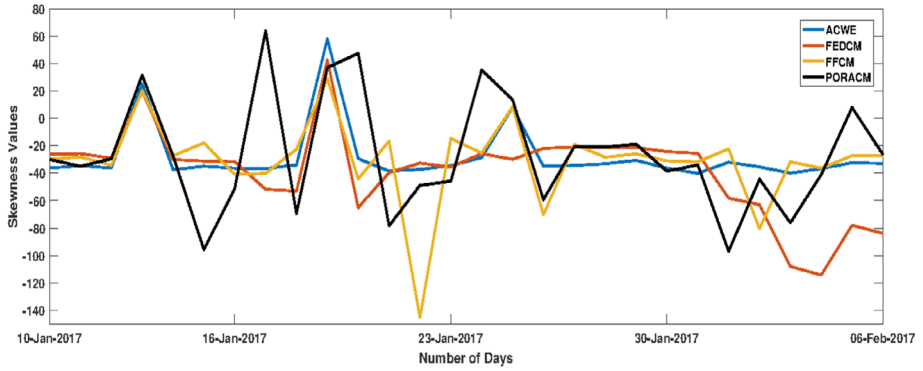

(b) Skewness of the flux distribution of magnetogram pixels values observed during a Carrington rotation.

Figure 9 Changes in the physical properties of the coronal holes with the change in Carrington rotation.

3.8. Analysis of CHs During Carrington Rotation

The physical properties of CHs and their corresponding phenomenons have also been analyzed during a particular solar Carrington rotation (CR) in this experiment. For this work, CR 2186[9] starting from *2017-01-10* and ending on *2017-02-06* has been considered. The corresponding HMI image has been obtained from the database of JSOC.[10] One SDO/AIA as well as HMI magnetogram of a solar image per day during the CR have been used. From the detected CHs region two parameters, namely the CHs area and magnetic flux distribution within the extracted CHs have been analyzed. CHs can be better understood on the basis of a nearly current-free coronal region with holes highlighting the open magnetic field (Wang and Sheeley, 1993). The variation in the physical parameter of segmented CHs with the variation of CR is shown in Figure 9. From the graph, it can be observed that all four compared methods of CHs segmentation show a similar variation for both parameters of the CHs under consideration.

[9]Data on Carrington rotation can be found in http://umtof.umd.edu/pm/crn/.

[10]SDO/HMI data has been collected from http://jsoc.stanford.edu/data/hmi/fits/.

From the graph of the percentage of CHs area in the solar disk, plotted in Figure 9a, it can be observed that during the initial stage of the CR all the four compared methods have detected approximately a similar low CHs area in the solar disk. The same trend can be seen at the end of the CR, where the CHs areas detected by the methods are low in percentage. It can also be seen that the CHs area attends its maximum during the period *2017-01-25* to *2017-01-31* of the CR. It indicates that the solar cycle is in its descending phase, as a sharp increase in the percentage of total CHs area corresponds to low solar activity during the period of CR (Minot, Lee, and Sun, 2018).

Furthermore, analyzing the graph of the skewness values of the magnetic flux during the CR given in Figure 9b, it can be concluded that during the descending phase of the solar cycle there is a large deep in the skewness value of the magnetic flux as generated by three compared methods. The skewness value was high during the initial stage of the CR, however, a sharp fall in the value of skewness can be noticed during the last stage of the CR. It can also be observed that during the initial stage of the CR the solar cycle had positive flux values, while at the last stage of CR the flux shifted to negative values. This could be attributed to the switching of the magnetic poles during the observed CR period (Minot, Lee, and Sun, 2018).

4. Conclusion

In this work a comparative analysis and the development of new contour-based techniques for segmentation of CHs region in the solar disk image have been carried out. In spite of various advantages the contour-based method of segmentation has a few constraints such as initial contour set-up, time complexity while solving optimization function, contour sticking at local minima. In order to handle these constraints and to solve the CHs segmentation problem in real time as a part of development, two contour-based techniques, namely POR-ACM and FFCM-SCM, have been proposed for the segmentation of CHs and compared with the existing FEDCM and ACWE method of CHs extraction. The first and vital advantage in both proposed techniques is that the methods do not need the gradient term to solve the optimization problem as required in the ACWE method of segmentation. As a consequence, the time complexity of the techniques gets reduced. Secondly, the implementation of circular Hough transform-based contour initialization as introduced in (Bandyopadhyay, Das, and Datta, 2020) addressed both the issue of limb correction and the contour initialization issue. This in turn avoids the requirement of the exact location of the solar disk center and accurate length of the solar disk radius (provided by the header of the *.fits* file) in order to handle the off-disk region in the solar disk image (Boucheron, Valluri, and McAteer, 2016). The circular Hough transform has the property to localize the shape of an object even in a noisy environment (Duda and Hart, 1972). Moreover, the proposed techniques do not require any separate technique as introduced in the work by Boucheron, Valluri, and McAteer (2016) or extra contour as initialized in (Bandyopadhyay, Das, and Datta, 2020) for off-disk region elimination purpose. The solar-limb pixels are removed automatically after the initialization of Hough transformed inspired circular disk. The morphological image processing method is working well even without magnetic field information in reducing the effect of filament channels in coronal hole detection, within low computational cost. However, some filament channels may still be included, in order to completely eliminate the effect of the filament channels further studies are needed and planned. The main motive behind the development two individual algorithms is to test whether newly developed single contour-based techniques can separately attain the same segmentation accuracy level within the real-time like

FEDCM or not. It is future work to combine the advantages of both POR-ACM and FFCM-SCM, in order to develop a modified fuzzy energy-based contour technique for CHs regions extraction in the solar disk image.

Acknowledgements The financial support received under the DST INSPIRE Faculty grant is thankfully acknowledged. We would also like to thank Dr. Laura Boucheron, Associate Professor, Klipsch School of Electrical and Computer Engineering, New Mexico State University, for her continuous support in this work. The authors thankfully acknowledge the use of data courtesy of NASA/SDO and the AIA and HMI science teams. The authors also thankfully acknowledge NOAA\SWPC. AD would like to acknowledge the support of EMR-II under CSIR No. 03(1461)/19.

Disclosure of Potential Conflicts of Interest The authors declare that they have no conflicts of interest.

Appendix: Contour Initialization and Limb Correction

The elimination of solar limbs in the process of CHs region detection is also a vital problem. The presence of solar limbs leads to the misclassification of the CHs region. The stated issue has been handled by introducing the circular Hough transform and the corresponding outcome is shown in Figures 11 and 12.

A.1 Contour Initialization in POR-ACM

An experiment has also been conducted for different contour initialization and using different ACM under various conditions. Among ACM, here mainly POR-ACM has been considered for its fastness in segmenting the image. After initializing the contour near the object boundary of the solar image, as shown in Figure 10b, then implementing POR-ACM without eliminating off-disk pixels for segmenting out CHs, it has been found that the method fails for the purpose. The method plotted the contour on the boundary of the CHs region and on the boundary of solar disk along with the portion of the solar limb. As such, regions outside the bigger contour having low-intensity value also have been selected as the CHs regions (as shown in Figure 10c). But as a piece of prior information, it is to be considered as a non-CH region. Also, in the upper portion of the solar disk in the image located in the first row of Figure 10c it can be seen that the low-intensity region has been considered as the background. This is due to the fact that when POR-ACM forces the contour to move towards the boundary of the RoI, it considers the intensity homogeneity information for evolving the contour, and in this case, the intensities of CHs region and solar image background are homogeneous. The same output can be found for the contour initialized within the solar disk and inside the RoI, as shown in Figures 10d–10g.

Now, after initializing the circular contour using the Hough transform (shown in Figure 11a), then applying POR-ACM without eliminating solar-limb and image background will generate the same results as shown in Figure 10c. This is due to the presence of the off-disk region (solar-limb and solar image background). Now, eliminating the off-disk region after initializing contour, as highlighted in Figure 11d, then again applying POR-ACM has failed to reach the boundary of the CHs. The corresponding results can be seen in Figure 11e. This is due to the property of ACM, which finds the minima in a local manner and as such the contour gets stuck on the edge of the solar disk. The force at the solar disk edge

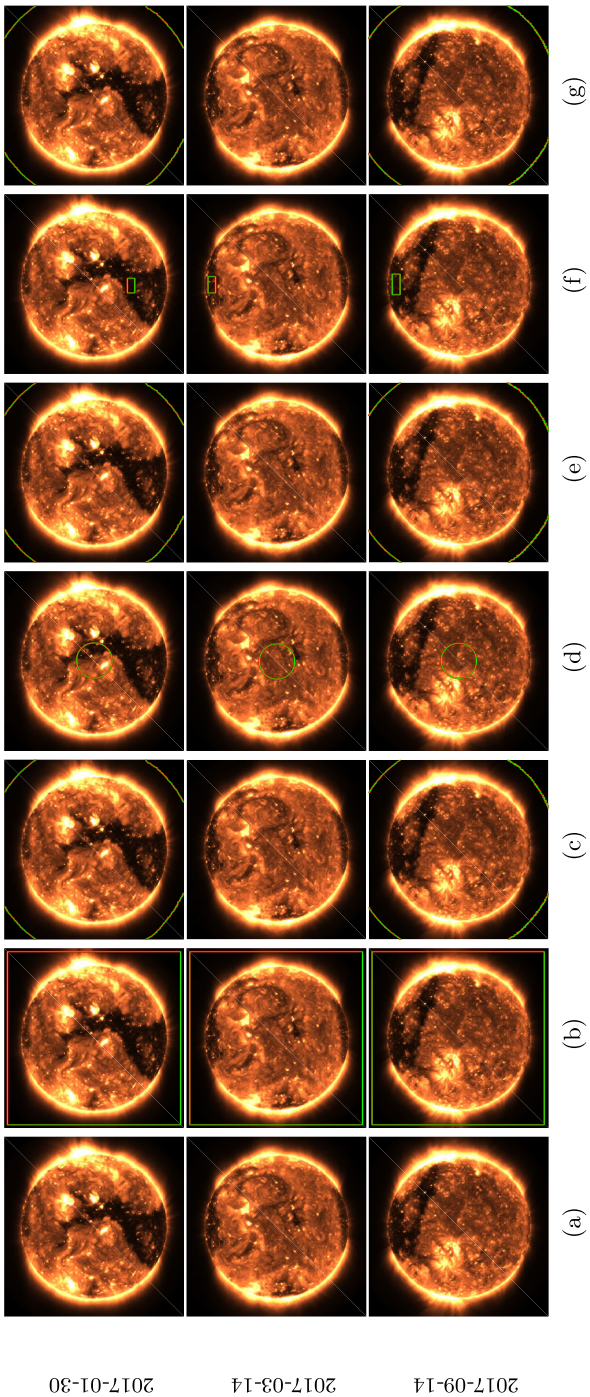

Figure 10 Different contour initialization and corresponding outputs obtained using POR-ACM without eliminating off-disk region have been shown, where original images are given in (**a**), contour initialization near image boundary shown in (**b**), and corresponding outputs have been shown in (**c**), contour initialization inside the solar disk has been displayed in (**d**) and corresponding outputs are given in (**e**), (**f**) show the contour set-up within the RoI and related outcomes are displayed in (**g**).

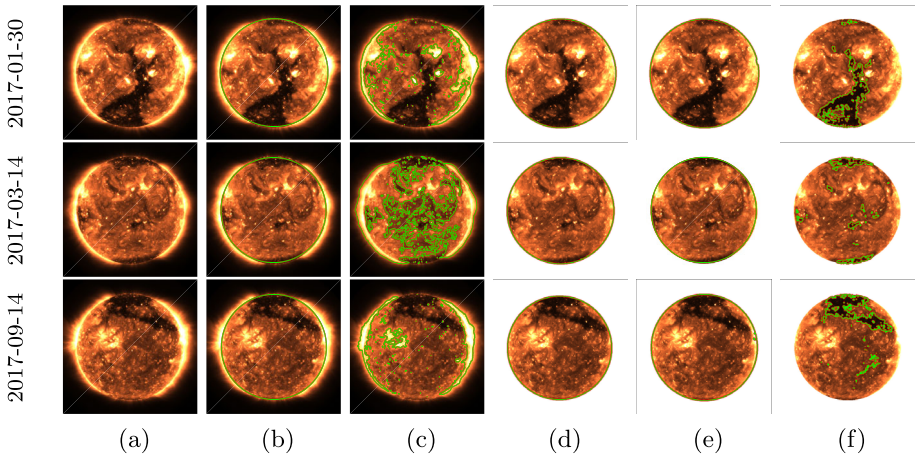

Figure 11 Various stages of POR-ACM-based CHs segmentation and contour initialization, where (**a**) original image, (**b**) initial contour, (**c**) results without eliminating off-disk region (**d**) elimination of off-disk region (**e**) output using OR-ACM after elimination and (**f**) final output using POR-ACM after elimination have been shown.

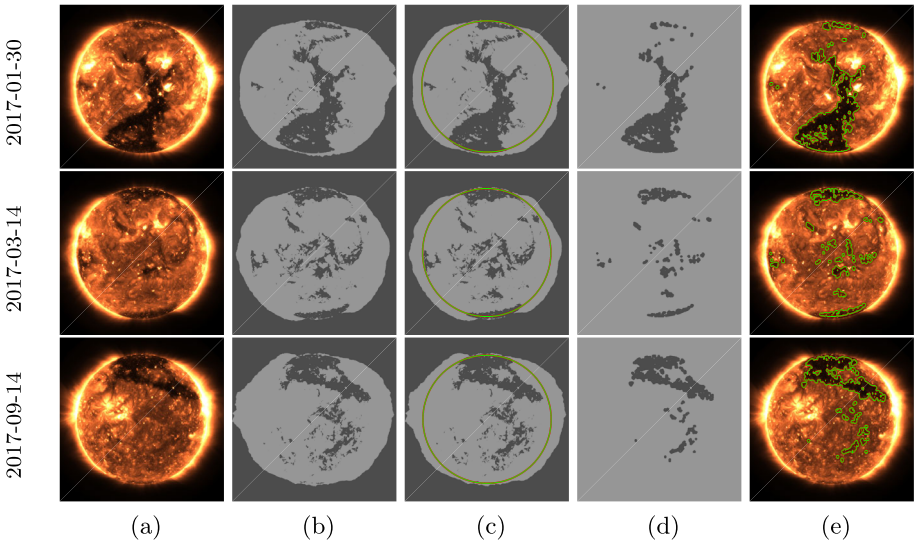

Figure 12 Various stages of FFCM-SCM-based CHs segmentation, where (**a**) original image, (**b**) output using FFCM, (**c**) static contour generation on FFCM results (**d**) Limb elimination and (**e**) final output have been shown.

is high due to the huge change in intensity value at the edge of solar disk. This force is preventing the contour to move further towards the CHs regions present inside the solar disk. However, after the application of the proposed POR-ACM, it can be found that the contour is able to reach the boundary of the CHs region as highlighted in Figures 2d and 11f. This is because the parameters in the introduced POR-ACM provide an extra force that overcomes the force extort by the change of intensity values at the edge of solar disk.

A.2 Contour Initialization in FFCM-SCM

From the second column of Figure 12, it can be seen easily that without the application of the solar-limb correction technique lead to the misclassification of the CHs region. The non-coronal holes regions present outside the solar disk region are also considered as CHs. Meanwhile, in the fourth column of the same figure it can be noticed easily that after the application of SCM employing a circular Hough transform based on the original image (as shown in Figure 12c) one has eliminated the problem of misclassification due to the presence of the off-disk region and has detected only the CHs region. This can also be established by the final outcome of the proposed technique shown in the last column of Figure 12. Basically, after the application of SCM the off-disk region is transformed into background or non-CHs region as given in Figure 12d. Thus, during this stage, the total image is left with only CHs regions (foreground) and non-CHs regions (background). As a consequence, the boundary of the CHs regions gets detected in the image. The final result can be seen in Figures 2e and 12e.

References

Bandyopadhyay, S., Das, S., Datta, A.: 2020, Fuzzy energy-based dual contours model for automated coronal hole detection in sdo/aia solar disk images. *Adv. Space Res.* **65**, 2435. DOI. http://www.sciencedirect.com/science/article/pii/S0273117720301046.

Barra, V., Delouille, V., Kretzschmar, M., Hochedez, J.-F.: 2009, Fast and robust segmentation of solar euv images: Algorithm and results for solar cycle 23. *Astron. Astrophys.* **505**, 361.

Bezdek, J.C., Ehrlich, R., Full, W.: 1984, Fcm: The fuzzy c-means clustering algorithm. *Comput. Geosci.* **10**, 191. DOI. http://www.sciencedirect.com/science/article/pii/0098300484900207.

Boucheron, L.E., Valluri, M., McAteer, R.T.J.: 2016, Segmentation of coronal holes using active contours without edges. *Solar Phys.* **291**, 2353. DOI.

Bresenham, J.E.: 1965, Algorithm for computer control of a digital plotter. *IBM Syst. J.* **4**, 25.

Caplan, R.M., Downs, C., Linker, J.A.: 2016, Synchronic coronal hole mapping using multi-instrument euv images: Data preparation and detection method. *Astrophys. J.* **823**, 53. DOI.

Caselles, V., Kimmel, R., Sapiro, G.: 1997, Geodesic active contours. *Int. J. Comput. Vis.* **22**, 61. DOI.

Chan, T.F., Vese, L.A.: 2001, Active contours without edges. *IEEE Trans. Image Process.* **10**, 266. DOI.

Ciecholewski, M.: 2015, Automated coronal hole segmentation from solar euv images using the watershed transform. *J. Vis. Commun. Image Represent.* **33**, 203. DOI. http://www.sciencedirect.com/science/article/pii/S1047320315001856.

Darolti, C., Mertins, A., Bodensteiner, C., Hofmann, U.G.: 2008, Local region descriptors for active contours evolution. *IEEE Trans. Image Process.* **17**, 2275. DOI.

Delouille, V., Hofmeister, S.J., Reiss, M.A., Mampaey, B., Temmer, M., Veronig, A.: 2018, Coronal holes detection using supervised classification. In: *Machine Learning Techniques for Space Weather* **365**, 978. ISBN 978-0-12-811788-0. DOI. http://www.sciencedirect.com/science/article/pii/B9780128117880000159.

Duda, R.O., Hart, P.E.: 1972, Use of the Hough transformation to detect lines and curves in pictures. *Commun. ACM* **15**, 11. DOI.

Gombosi, T.I.: 1998, *Physics of the Space Environment*, *Cambridge Atmospheric and Space Science Series*. Cambridge University Press, Cambridge. DOI.

Harvey, K.L., Recely, F.: 2002, Polar coronal holes during cycles 22 and 23. *Solar Phys.* **211**, 31. DOI.

Hough, P.V.: 1962, Method and means for recognizing complex patterns. Google Patents. US Patent 3,069,654.

Huang, C., Zeng, L.: 2015, An active contour model for the segmentation of images with intensity inhomogeneities and bias field estimation. *PLoS ONE* **10**, e0120399.

Illarionov, E.A., Tlatov, A.G.: 2018, Segmentation of coronal holes in solar disc images with a convolutional neural network. *Mon. Not. Roy. Astron. Soc.* **481**, 5014. DOI.

Kirk, M.S., Pesnell, W.D., Young, C.A., Webber, S.H.: 2009, Automated detection of euv polar coronal holes during solar cycle 23. *Solar Phys.* **257**, 99.

Krinidis, S., Chatzis, V.: 2009, Fuzzy energy-based active contours. *IEEE Trans. Image Process.* **18**, 2747. DOI.

Krista, L.D., Gallagher, P.T.: 2009, Automated coronal hole detection using local intensity thresholding techniques. *Solar Phys.* **256**, 87. DOI.

Lowder, C., Qiu, J., Leamon, R., Liu, Y.: 2014, Measurements of euv coronal holes and open magnetic flux. *Astrophys. J.* **783**, 142.

Minot, A.D., Lee, J., Sun, X.: 2018, Analysis of coronal holes in the descending phase of cycles 23 and 24 using EUV and magnetic field data. In: *AGU Fall Meeting Abstracts 2018*, SH43F. ADS.

Munro, R.H., Withbroe, G.L.: 1972, Properties of a coronal "hole" derived from extreme-ultraviolet observations. *Astrophys. J.* **176**, 511.

Nieniewski, M.: 2004, Extraction of diffuse objects from images by means of watershed and region merging: Example of solar images. *IEEE Trans. Syst. Man Cybern., Part B, Cybern.* **34**, 796. DOI.

Reiss, M.A., Hofmeister, S.J., De Visscher, R., Temmer, M., Veronig, A.M., Delouille, V., Mampaey, B., Ahammer, H.: 2015, Improvements on coronal hole detection in sdo/aia images using supervised classification. *J. Space Weather Space Clim.* **5**, A23. DOI.

Reiss, M., Temmer, M., Rotter, T., Hofmeister, S., Veronig, A.: 2014, Identification of coronal holes and filament channels in sdo/aia 193Å images via geometrical classification methods. *Cent. Eur. Astrophys. Bull.* **38**, 95.

Rotter, T., Veronig, A.M., Temmer, M., Vršnak, B.: 2012, Relation between coronal hole areas on the sun and the solar wind parameters at 1 au. *Solar Phys.* **281**, 793. DOI.

Semechko, A.: 2019, Fast fuzzy c-means image segmentation. GitHub.

Talu, M.F.: 2013, Oracm: Online region-based active contour model. *Expert Syst. Appl.* **40**, 6233. DOI. http://www.sciencedirect.com/science/article/pii/S0957417413003540.

Verbeeck, C., Delouille, V., Mampaey, B., De Visscher, R.: 2014, The spoca-suite: Software for extraction, characterization, and tracking of active regions and coronal holes on euv images. *Astron. Astrophys.* **561**, A29.

Wang, Y.-M., Sheeley, J.N.R.: 1993, Understanding the rotation of coronal holes. *Astrophys. J.* **414**, 916. DOI. ADS.

Wang, L., Chang, Y., Wang, H., Wu, Z., Pu, J., Yang, X.: 2017, An active contour model based on local fitted images for image segmentation. *Inf. Sci.* **418–419**, 61. DOI. http://www.sciencedirect.com/science/article/pii/S0020025516308556.

Xie, X., Mirmehdi, M.: 2010, Initialisation-free active contour segmentation. In: *2010 20th International Conference on Pattern Recognition*, 2318. DOI.

Xingfei, G., Jie, T.: 2002, An automatic active contour model for multiple objects. In: *Object Recognition Supported by User Interaction for Service Robots* **2**, 881.

Yuen, H., Princen, J., Illingworth, J., Kittler, J.: 1990, Comparative study of hough transform methods for circle finding. *Image Vis. Comput.* **8**, 71.

Zhang, K., Zhang, L., Song, H., Zhou, W.: 2010, Active contours with selective local or global segmentation: A new formulation and level set method. *Image Vis. Comput.* **28**, 668. DOI. http://www.sciencedirect.com/science/article/pii/S0262885609002303.